Acta Oceanol. Sin., 2024, Vol. 43, No. 10, P. 16–32
https://doi.org/10.1007/s13131-024-2353-4
http://www.aosocean.com
E-mail: ocean2@hyxb.org.cn

Influence of mixed layer depth on chlorophyll-*a* concentration in the Southern Ocean

Yuxin Shi[1], Hailong Liu[2]*, Quanan Zheng[3]

[1] School of Oceanography, Shanghai Jiao Tong University, Shanghai 200240, China

[2] Yunnan Key Laboratory of Meteorological Disasters and Climate Resources in the Greater Mekong Subregion, Yunnan University, Kunming 600650, China

[3] Department of Atmospheric and Oceanic Science, University of Maryland at College Park, College Park 20742, USA

Received 10 December 2023; accepted 29 April 2024

Abstract

The element iron limitation is one of the crucial factors contributing to high nutrient low chlorophyll in the Southern Ocean (SO). Mixed layer dynamics regulate the availability of iron to phytoplankton. In this paper, we investigate the influence of surface iron supplementation triggered by the mixed layer depth (MLD) variation on chlorophyll-*a* (Chl-*a*) concentration in the SO on seasonal and interannual timescales. This analysis is based on the Biogeochemical Southern Ocean State Estimate for the period from 2013 to 2021. We provide a comprehensive and systematic mapping of the regions within the SO, where Chl-*a* is affected by iron input related to MLD deepening. The relationship between the MLD and the Chl-*a* varies with the latitude on the seasonal time scale. Both the MLD and sea ice melting affect the distribution of Chl-*a*. On the interannual scale, iron supply due to MLD deepening occurs primarily north of 60°S. Horizontal advection-induced entrainment enhances the surface iron input during the austral summer, which favors Chl-*a* increase. In addition to the MLD, the melting of sea ice and cooling of the sea surface can also alter iron input and subsequently affect Chl-*a* distribution in the austral summer. During the austral winter, entrainment can boost iron stocks, stimulating a subsequent spring increase of Chl-*a* in the SO. Furthermore, sea surface temperature declines during the austral winter, promoting an increased iron supply and creating favorable conditions for the subsequent spring Chl-*a* increase in the SO.

Key words: mixed layer depth, entrainment, chlorophyll-*a* concentration, Southern Ocean

Citation: Shi Yuxin, Liu Hailong, Zheng Quanan. 2024. Influence of mixed layer depth on chlorophyll-*a* concentration in the Southern Ocean. Acta Oceanologica Sinica, 43(10): 16–32, doi: 10.1007/s13131-024-2353-4

1 Introduction

The Southern Ocean (SO), the largest ocean in the world, plays a vital role in global climate regulation through biological pumps and solubility (Boyd and Ellwood, 2010; Marinov et al., 2008; Martin et al., 1990a). This region is characterized by high nutrient low chlorophyll (HNLC), which is mainly affected by the element iron and light limitation (Boyd et al., 1999; Boyd, 2002; Fauchereau et al., 2011; Martin et al., 1990b). Generally, macronutrients such as nitrate and phosphate do not affect phytoplankton growth in the SO. Despite the marked HNLC conditions in the SO, phytoplankton blooms are observable during the spring and summer seasons (Blain et al., 2007; Carranza and Gille, 2015; Frants et al., 2013; Korb et al., 2008). Phytoplankton blooms generally occur near ocean fronts, continental shelves, marginal ice zones, major islands, and polynyas, which align with identified iron sources (Arrigo and Van Dijken, 2003; Arrigo et al., 2008; Blain et al., 2007; Geibert et al., 2010; Graham et al., 2015; Park et al., 2010). In addition to dust deposition, river runoff, anoxic coastal sediments, and sea-ice melting, vertical iron transport from subsurface waters to the surface also represents a significant source of iron supply (Fauchereau et al., 2011; Tagliabue et al., 2014). Given that the SO is unrestricted by light for at least three months of the year (Venables and Moore, 2010), persistent phytoplankton blooms may necessitate a continuous iron supply from the subsurface to surface waters. Therefore, the physical processes that trigger vertical transport in the ocean become very important. On the other hand, chlorophyll-*a* (Chl-*a*) concentration is a widely used indicator for characterizing phytoplankton biomass and is key to photosynthesis (Arrigo et al., 2008; Moline et al., 2004). High concentrations of Chl-*a* typically signify a greater abundance of phytoplankton and algae (Moore and Abbott, 2000). Phytoplankton are the primary producers in marine ecosystems, forming the basis of the food chain. The distribution of predators is intricately linked to that of Chl-*a*. The distribution of Chl-*a* can impact primary productivity and even affect the entire ecosystem through the food chains and food webs (Pauly and Christensen, 1995). Consequently, a comprehensive study of the effects of iron input linked to mixed layer depth (MLD) variations on Chl-*a* is essential.

Previous studies have indicated that winter deep mixing or entrainment, Ekman upwelling, and vertical diapycnal diffusion are the primary physical processes involved in the vertical supply of dissolved iron (De Baar et al., 1995; Moore et al., 2001). Tagliabue et al. (2014) utilized observational data and dissolved

Foundation item: The fund from Ministry of Science and Technology of the People's Republic of China under contract No. 2023YFF0805204; the Natural Science Foundation of Yunnan Province under contract No. 202302AN360006; the National Natural Science Foundation of China under contract No. 41776019.
*Corresponding author, E-mail: hailong.liu@ynu.edu.cn

iron profiles to examine the relative contributions of diapycnal diffusion and deep winter mixing (entrainment) to dissolved iron fluxes in the SO. Their findings indicate that deep winter mixing supplies ten times more iron to the surface ocean annually than diapycnal diffusion. The SO mixed layer (ML) thus plays a unique and important role in regulating Chl-*a* via the modulation of the vertical supply of dissolved iron, especially in winter (Mitchell et al., 1991; Sallée et al., 2010). In addition, various physical processes, including fronts, eddies, and lateral transport from shelf regions, contribute to the supply of iron to the euphotic zone (Hense et al., 2000; Moore et al., 2004; Taylor and Ferrari, 2011; Tripathy et al., 2015). However, this study exclusively concentrates on the physical processes governing the vertical transport of iron from the subsurface to the surface by ML dynamics.

The relationship between the MLD and the Chl-*a* is intricate and nonlinear. For example, assuming the MLD is sufficiently deep, its further deepening has almost no effect on the availability of light. Conversely, if the MLD is shallow enough to be entirely exposed to sunlight, a slight change can lead to significant changes in phytoplankton biomass (Boyd et al., 2000; Sallée et al., 2010). A positive correlation often exists between the MLD and the Chl-*a* in well-lit, nutrient-limited extrapolar regions. It suggests that entrainment caused by MLD deepening encourages iron supply from the subsurface to the surface layer (Bowie et al., 2015; McGillicuddy et al., 2015). However, at high latitudes, the MLD and the Chl-*a* show a negative correlation, which indicates that a high Chl-*a* level is simultaneously changing with the shallow MLD (Fauchereau et al., 2011). In high-latitude regions with stringent light conditions (south of 40°S), iron is not a significant factor in limiting Chl-*a* increase (Martin et al., 1990b; Tagliabue et al., 2014). Phytoplankton growth within the ML is more susceptible to variations in light conditions. A deeper MLD results in decreased light availability, thus limiting phytoplankton photosynthesis. When the MLD exceeds the critical depth, a fraction of the phytoplankton contained within it is unable to undergo photosynthesis and fails to bloom (Mitchell et al., 1991; Sverdrup, 1953). Hence, a shallow MLD is crucial for preserving the increase of Chl-*a*, which explains the negative correlation between the two. In the broad open ocean, strong winds are associated with elevated Chl-*a* levels, suggesting that MLD deepening caused by wind-driven entrainment helps sustain elevated Chl-*a*. The MLD deepening resulting from wind-driven entrainment plays a dominant role on time scales of several days (Carranza and Gille, 2015).

In general, seasonal iron stocks are mainly replenished from below ferricline due to the deep MLD in the SO during winter. However, the low mean light level in ML results in a correspondingly low phytoplankton growth level south of the subtropical front (Arrigo et al., 2008; Fauchereau et al., 2011). The MLD gradually becomes shallower during the transition from winter to spring, which alleviates light limitation. In addition, MLD shoaling and stratification enhancement during seasonal transitions retain iron on the surface. The processes of increasing light and iron inputs at the sea surface both favor phytoplankton growth (Boyd et al., 1999; Boyd, 2002; Li et al., 2021). Due to the continuous depletion in spring, the iron stocks are almost depleted in the subsequent summer and iron limitation occurs. As a result, phytoplankton growth rates decline until all iron is depleted (Boyd et al., 1999). On the interannual time scale, the deepening of the MLD also plays a significant role in the spatial distribution of Chl-*a*. Deep winter mixing contributes to phytoplankton blooms in the subsequent growing season (spring), as a consequence of the entrainment of iron into the euphotic zone (Fauchereau et al., 2011; Tagliabue et al., 2014; Thomalla et al., 2011).

In addition to iron inputs resulting from MLD variations, sea ice formation and retreat can also affect iron availability and thus alter phytoplankton growth. It is widely recognized that the melting of sea ice plays a pivotal role in replenishing iron in the SO. The iron released by the melting of ice shelves, glaciers, and drifting icebergs could potentially fertilize nearby waters. Additionally, ice-free land areas may expand as sea ice retreats, potentially contributing to enhanced flux of iron to sea ice via dust deposition. Sea ice formation has a dual effect on phytoplankton growth. Convection caused by brine rejection during sea ice formation promotes iron input at the surface. However, extensive sea ice formation inhibits the entrance of light to the sea surface. According to related model studies, iron is found to be stored in ice during the winter formation and subsequently transported through ice motion. It is then released and available to phytoplankton during the summer melt (Lancelot et al., 2009). The residence time of dissolved iron in the upper ocean varies from several years to a decade. The sustainability of the subsurface iron pool is heavily reliant on continual replenishment from atmospheric dust deposition (Moore et al., 2004). These findings corroborate the potential significance of iron sources and transport in the Southern Ocean in shaping the geographic development of phytoplankton blooms and associated ecosystems.

The spatial distribution of Chl-*a* in the SO coincides with the iron limitation regime and the iron input is primarily derived from ML entrainment, which has been well documented (De Baar et al., 1995; Boyd et al., 1999, 2000; Fauchereau et al., 2011; Li et al., 2021; Tagliabue et al., 2014). However, the process of phytoplankton growth is intricate and localized. It remains unclear whether all of the increased iron input from entrainment can be used to increase Chl-*a*. Furthermore, the physical mechanisms that are responsible for entrainment are also uncertain. The deepening of MLD may not necessarily entrain iron into the euphotic layer. Therefore, this study aims to delineate a schematic for effective MLD deepening on different time scales (seasonal and interannual) by examining the relationships among MLD, Chl-*a*, and iron. The effective MLD deepening means that not only does entrainment increase iron inputs, but all of these iron inputs are devoted to the increase of Chl-*a*. Based on the preceding discussion, the physical processes that induce effective entrainment are further investigated.

The remainder of this paper is organized as follows: Section 2 provides a brief description of the dataset and methods. Section 3 gives data validation, comparing the observational data with the data in this paper to assess the availability of the data used in this paper. Section 4 and Section 5 investigate the regions and mechanisms of effective MLD or entrainment on seasonal and interannual timescales, respectively. Finally, the discussion and conclusions are given in Section 6.

2 Dataset and methods

2.1 *Dataset*

This study utilizes monthly Biogeochemical Southern Ocean State Estimate (B-SOSE) data. The data has a resolution of (1/6)°, with 52 vertical layers, ranging from January 2013 to December 2021. The B-SOSE model incorporates light, iron, nutrients, and gas models based on the SOSE, which is a coupled biogeochemical-sea ice-ocean state estimation model for the SO (Galbraith et al., 2010; Mazloff et al., 2010; Verdy and Mazloff, 2017). The B-SOSE model includes sea-air fluxes of heat and carbon and nutri-

ent cycling. There are eight biochemical tracers, which include dissolved inorganic carbon (DIC), alkalinity (ALK), iron (Fe), phosphate (PO_4), nitrate (NO_3), oxygen (O_2), and dissolved organic matter (DON, DOP). Although the model incorporates a relatively small number of parameters, it encompasses key biogeochemical processes that impact phytoplankton, including nutrient uptake and remineralization, changes in alkalinity and oxygen, and the cycling of iron and organic matter. Meanwhile, B-SOSE assimilates all available observations, making Chl-*a* and iron in this study more credible and closer to real observations. The iron covers all possible natural sources. The variables used in this study comprise temperature, salinity, Chl-*a*, sea ice concentration (SIC), and dissolved inorganic iron concentration. The temperature and salinity data are utilized to calculate the MLD.

The reliability of the MLD derived from B-SOSE is validated using the World Ocean Database 2018 (WOD18) observational dataset (Boyer et al., 2019). All available profiles from 2013 to 2018 are used, including high-resolution conductivity temperature depth (CTD), moored buoys mainly from the Equatorial buoy arrays-TAO (MRB), Gliders (GLD), and Profiling floats (PFL). The extensive coverage provided by the dataset enables us to obtain monthly maps of the MLD at a 1° grid resolution. The monthly Chl-*a* data is derived from the visible infrared imaging radiometer suite (VIIRS) sensor (Schueler et al., 2002), which is a crucial instrument onboard Suomi National Polar-orbiting Partnership (Suomi NPP). The spatial resolution of the dataset is 9 km × 9 km, spanning the period from January 2013 to December 2021. These observational data are utilized to examine the reliability of Chl-*a* derived from B-SOSE.

2.2 *MLD estimation*

The MLD is defined as the shallowest layer among the isothermal, isopycnic, and isohaline layers, according to Helber et al. (2012). This method accurately captures the MLD and ensures a uniform distribution of physical variables within this layer. To facilitate effective comparison, the isothermal, isopycnic, and isohaline layer depths are all obtained based on the temperature difference of 0.2℃ (ΔT, temperature threshold). The optimal threshold is 0.2℃, which is considered the most appropriate estimation from individual profiles and has been used widely in previous studies (Carton et al., 2008; Dong et al., 2008; De Boyer Montégut et al., 2004; Qiu et al., 2012; Shi et al. 2024; Ying et al., 2019). The formulas of density threshold ($\Delta\theta$) and salinity threshold (ΔS) are as follows:

$$\Delta\theta = \theta\left(T_{10} - \Delta T, S_{10}, P_0\right) - \theta\left(T_{10}, S_{10}, P_0\right), \tag{1}$$

$$\Delta S = 0.01n, \quad n = 1, 2, \cdots, \tag{2}$$

$$\Delta\theta_s = \theta\left(T_{10}, S_{10} + \Delta S, P_0\right) - \theta\left(T_{10}, S_{10}, P_0\right), \tag{3}$$

$$\Delta\theta_s = \Delta\theta, \tag{4}$$

where T_{10} and S_{10} represent the potential temperature and salinity at a reference depth of 10 m, respectively, P_0 refers to the pressure at the surface of the ocean which is taken to be 0. ΔT is equal to 0.2℃ as mentioned above.

2.3 *Entrainment rate of MLD*

To examine the impact of MLD entrainment on Chl-*a* distribution, the entrainment rate, w, is calculated. The equation causing the entrainment effect is presented as follows (Chu, 1993; Chu and Garwood, 1991; Chu et al., 1990; Ma et al., 2021; Pang et al., 2019):

$$w = \begin{cases} \dfrac{\partial h}{\partial t} + w_b + \boldsymbol{V}\cdot\nabla h, & \dfrac{\partial h}{\partial t} + w_b + \boldsymbol{V}\cdot\nabla h > 0, \\ 0, & \text{otherwise}, \end{cases} \tag{5}$$

where $\dfrac{\partial h}{\partial t}$ denotes the rate of MLD deepening, h is the MLD, w_b is the vertical velocity at the ML base, $\boldsymbol{V}$ is the horizontal velocity, and ∇ is the divergence operator, $\boldsymbol{V}\cdot\nabla h$ indicates the horizontal advection of water in the ML.

3 B-SOSE data validation

Before examining the correlation between MLD and Chl-*a*, it is essential to ascertain the robustness and reliability of the MLD and Chl-*a* data derived from the B-SOSE. The validation of B-SOSE MLD is executed using the observational data from WOD18. The Chl-*a* from the VIIRS sensor is employed to validate the B-SOSE Chl-*a* data. The climatological MLDs of B-SOSE and WOD18 are shown in Fig. 1. Note that since the MLD in WOD18 is only available until 2018, the MLD from B-SOSE is only retained until 2018 for valid comparison between the two datasets. In general, although the magnitude of the B-SOSE MLD is smaller than that of the WOD18 MLD, the B-SOSE MLD captures the seasonal variation characteristics well. Both datasets show similar spatial distribution characteristics. Specifically, the MLD from B-SOSE is the deepest in the austral winter (JJA), exceeding 200 m. The deep MLD region occurs mainly between 40°S and 60°S showing a zonal distribution. Compared to this deep MLD band, the MLD north of 40°S is shallower, reaching a depth of only 80 m (Fig. 1d). The deep MLD band during austral spring (SON) still maintains a relatively deep level. However, the MLD north of 40°S becomes shallower than that during the austral winter, with a magnitude of 50 m (Fig. 1a). The shallowest MLD can be observed in the austral summer (DJF), with the entire SO exhibiting a depth shallower than 100 m (Fig. 1b), and the deep MLD band almost disappears. During the subsequent autumn (MAM), the deep MLD band reappears, but the MLD north of 40°S remains shallow (Fig. 1c). Furthermore, the MLD is consistently less than 50 m in depth throughout the year in the vicinity of Antarctica (Figs 1a–d). The MLD derived from WOD18 shows similarity with B-SOSE MLD, except that the MLD is deeper north of 40°S during the austral autumn. It is also observed that observational data are scarce in the vicinity of Antarctica.

Figure 2 shows the seasonal evolution of Chl-*a* concentration derived from the B-SOSE and VIIRS. Generally, the two datasets indicate similar spatial distribution of Chl-*a*. However, the B-SOSE underestimates Chl-*a*. The distribution of B-SOSE Chl-*a* shows significant seasonal variations. The austral spring and summer are regarded as the growth seasons of phytoplankton in the SO. High Chl-*a* level, with a value of 0.1 mg/m^3, is observed in the Antarctic, islands, and near the coast, particularly during the austral summer (Figs 2a and b). In the austral autumn and winter, Chl-*a* is reduced, especially in the austral winter. Chl-*a* in the vicinity of Antarctica is below 0.03 mg/m^3 in the austral winter (Figs 2c and d). Meanwhile, the Pacific sector exhibits a consistently low Chl-*a* level throughout the year, but the Atlantic sector is relatively high. For the Chl-*a* from satellite data, it is higher all year round. The distribution features are identical to those of B-SOSE, indicating a peak of Chl-*a* in the austral summer and a decline in the austral winter (Figs 2f and h). Throughout the year,

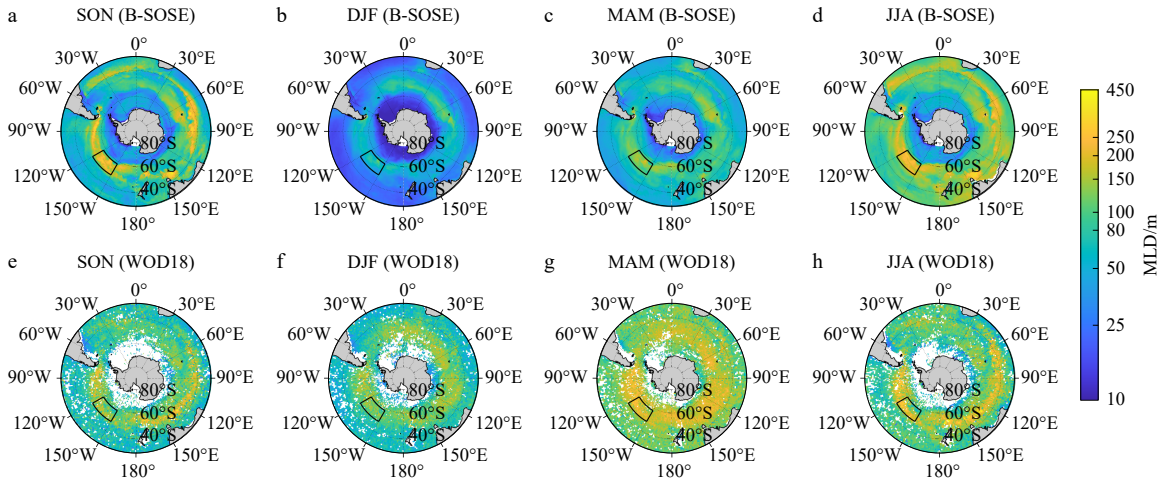

Fig. 1. Seasonal cycle of MLD from B-SOSE (a–d) and WOD18 (e–h). The values represent the climatological mean over the period during 2013 to 2018. A region within the deep MLD band is randomly selected to test the credibility of B-SOSE (black box in Fig. 1). The seasons are defined as spring including March, April, and May (MAM), summer including June, July, and August (JJA), autumn including September, October, and November (SON) and winter including December, January, and February (DJF).

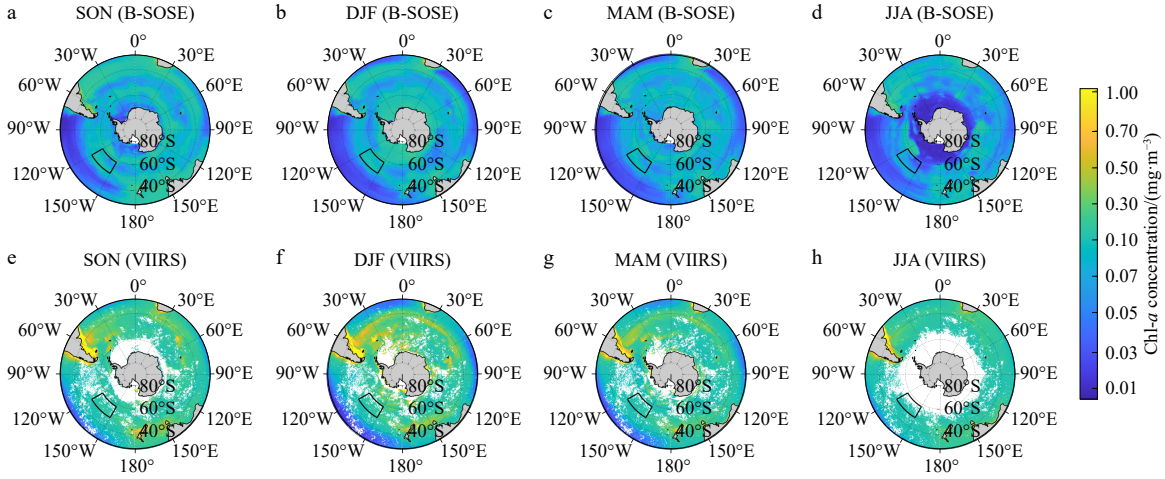

Fig. 2. Seasonal cycle of Chl-*a* concentration from B-SOSE (a–d) and VIIRS (e–h) sensor. The values represent the climatological mean over the period from 2013 to 2021. The black box in the subplot represents the same region as the black box in Fig. 1.

the Chl-*a* remains low (<0.1 mg/m^3) in the Pacific sector, whereas it remains relatively high (>0.3 mg/m^3) in the Atlantic sector.

To ascertain the suitability of the MLD derived from B-SOSE for an interannual timescale study, the area-averaged time series of MLD anomaly from B-SOSE and WOD18 are presented in Fig. 3. A region within the deep MLD band is randomly selected to test the credibility of B-SOSE (black box in Fig. 1). The difference between the two datasets is mainly found in 2015, 2016, and 2018. However, the MLD of the two datasets are highly correlated (r = 0.77, p < 0.000 1). In addition, other areas within the deep MLD band have also been investigated. The B-SOSE has shown a good correlation with WOD18 data (not shown). This indicates that the B-SOSE can effectively simulate the variation characteristics of MLD on the interannual time scale.

Figure 4 shows the time series of the Chl-*a* anomaly derived from the B-SOSE and the VIIRS sensor in the black box. Similarly to the MLD, the Chl-*a* from the two datasets exhibits a disparity in magnitude, yet a satisfactory correlation of 0.50 (p < 0.000 1) is observed. The correlation of Chl-*a* derived from the two datasets is also validated by other boxes in critical regions (deep MLD band). The results demonstrate that the significant correlation is robust across boxes. Additionally, due to the sea ice cover in the austral winter, Chl-*a* from VIIRS is absent, and B-SOSE can compensate for this deficiency. Despite differences in values, B-SOSE

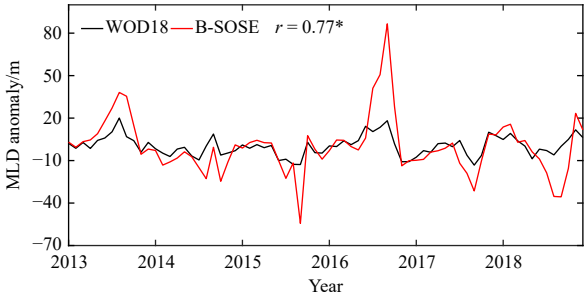

Fig. 3. Time series of monthly MLD anomaly from B-SOSE and WOD18. The values are calculated by the black box depicted in Fig. 1. The asterisk (*) represents that the results are statistically significant at the 95% confidence level.

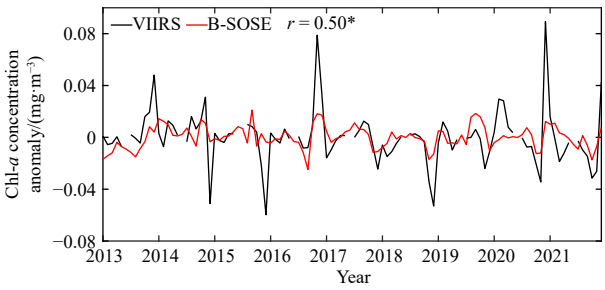

Fig. 4. Time series of monthly Chl-*a* anomaly derived from B-SOSE and VIIRS sensor. The values are calculated by the black box depicted in Fig. 2. The asterisk (*) represents that the results are statistically significant at the 95% confidence level.

effectively captures the spatial characteristics of seasonal MLD and Chl-*a* evolution (Figs 1 and 2). On the interannual scale, the MLD derived from B-SOSE and WOD18, as well as the Chl-*a* derived from B-SOSE and satellite, exhibit a high correlation in key regions (Figs 3 and 4). This indicates that B-SOSE is reliable and valid for seasonal and interannual scale analysis. Furthermore, B-SOSE can alleviate the temporal and spatial limitations of observational data. It should be noted that the mean state may affect the variability of the MLD and Chl-*a*, but here we assume that it does not affect the results.

4 Relationship between MLD and Chl-*a* on the seasonal time scale

The last section confirms the availability of B-SOSE data and provides a preliminary understanding of the seasonal variation of MLD and Chl-*a*. To further understand the climatological characteristics of MLD and Chl-*a*, the statistics of the maximum value of the two variables and the corresponding occurrence month are shown in Fig. 5. One can see that the characteristics of the maximum MLD are very similar to austral winter MLD in both magnitude and pattern (Figs 1d and 5a). The maximum MLD tends to be concentrated in July–September (austral winter and spring). It is notable that a ring exists near 60°S, where the MLD reaches its maximum in May (austral autumn), preceding than other regions of the SO (Figs 5b and c). This ring is located precisely on the edge of the sea ice, which suggests that the presence of sea ice obstructs the wind from stirring and mixing the upper layers. The strong winter winds here thus do not form the deeper MLD. The Chl-*a* reaches its peak during the austral summer south of 60°S and the austral spring north of 60°S (Fig. 5f), consistent with previous results (Fauchereau et al., 2011; Thomalla et al., 2011). Furthermore, the maximum Chl-*a* in the East Pacific sector is less than 0.1 mg/m³ (Fig. 5d). The maximum Chl-*a* in this area occurs in July–September (Figs 5e and f, austral winter and spring). The Chl-*a* loss rate is lower than the growth rate due to the dilution effect of the deepening MLD on herbivores, therefore the Chl-*a* increases in the austral winter and spring (Behrenfeld et al., 2013).

A comparison of the timing of MLD and Chl-*a* maxima in Fig. 5 reveals that the Chl-*a* maximum typically occurs after the MLD maximum, except in the East Pacific. This suggests that MLD deepening may influence the distribution of Chl-*a*, and such an effect could be instantaneous or lagged. To further investigate the impact of MLD deepening on the Chl-*a* level and the response time of Chl-*a* to this effect, we calculate the instantaneous correlation between MLD and Chl-*a*. Additionally, we determined the correlation coefficients of Chl-*a* lagging MLD for 1–6 months, respectively (not shown). The strongest positive and negative correlation coefficients are identified for each grid, and the lag time of Chl-*a* when the strongest correlation coefficient appears is recorded. The results are presented in Fig. 6.

Figures 6a–c illustrate the highest positive correlation coefficient between the MLD and Chl-*a* under climatological conditions, as well as the corresponding lag time. Although a significant positive correlation is present throughout the SO, the lag time of Chl-*a* varies at different latitudes. Previous studies (Fauchereau et al., 2011; Tagliabue et al., 2014) have indicated that when the MLD and Chl-*a* reach the strongest correlation, the lag time of Chl-*a* can be classified as instantaneous correlation if it ranges from 0 month to 2 months, one-season lag for 3 months to 4 months, and half-year lag for 5 months to 6 months as illustrated in Fig. 6c. Consequently, the positive correlation between the MLD and Chl-*a* can be divided into three broad zonal regions in the SO as follows: (1) the instantaneously correlated region at low latitudes (blue color in Fig. 6c, hereafter referred to as Region P1); (2) the mid-latitude region where Chl-*a* lags behind MLD by one season (yellow color in Fig. 6c, hereafter referred to as Region

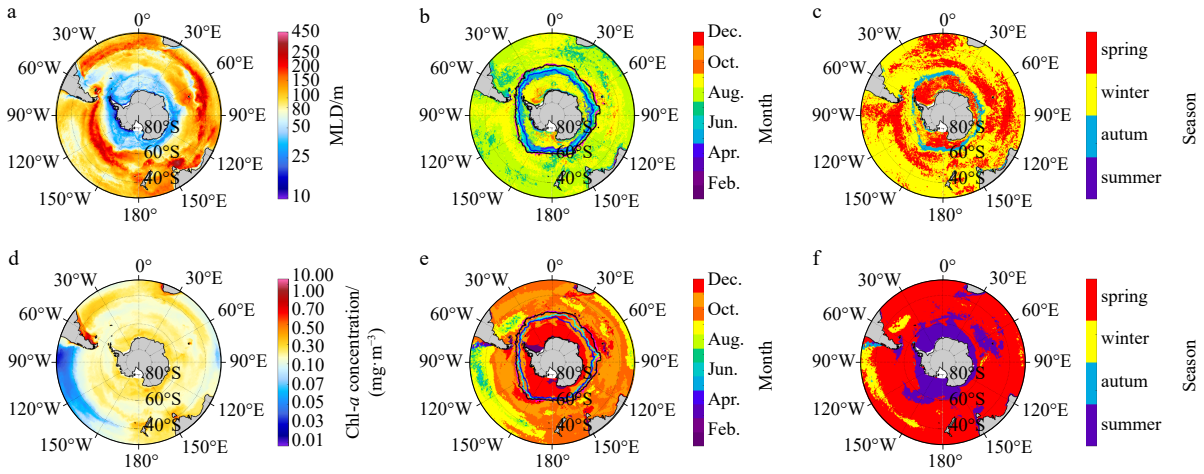

Fig. 5. Maximum values of MLD (a) and Chl-*a* (d) and the occurrence time of maximum MLD (b, c) and Chl-*a* (e, f) from B-SOSE. b and e show the months when the maximum value occurs, c and f show the seasons when the maximum value occurs. In c and f, the colored contours represent the edges of sea ice in four seasons: the black, cyan, blue, and pink contours represent austral spring, summer, autumn, and winter, respectively.

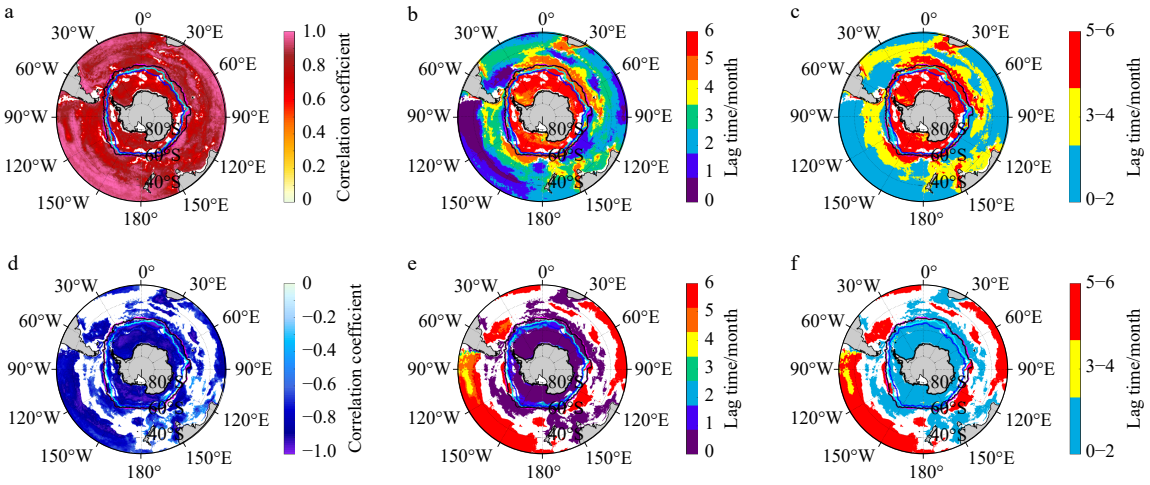

Fig. 6. Strongest positive (a) and negative (d) correlation coefficients between the MLD and Chl-*a* and the time that Chl-*a* lags the MLD when the strongest correlation coefficient occurs (b, c, e, f). Figures 6a and d are statistically significant, and the statistically insignificant points have been removed. The colored contours represent the edges of sea ice in four seasons. The black, cyan, blue, and pink contours represent austral spring, summer, autumn, and winter, respectively.

P2), mainly between 40°S and 60°S; and (3) the region in the high latitudes where Chl-*a* lags behind MLD by half a year under sea ice (red color in Fig. 6c, hereafter referred to as Region P3). Similarly, the SO can be classified into three regions based on the negative correlation between the two and the time lag of Chl-*a* (Figs 6d and 6e), as shown in Fig. 6f. The three regions are as follows: (1) the instantaneously correlated region at mid and high latitudes (blue color in Fig. 6f, hereafter referred to as Region N1); (2) the region where Chl-*a* lags behind the MLD by one season in the East Pacific (yellow color in Fig. 6f, hereafter referred to as Region N2); and (3) the region where Chl-*a* lags behind the MLD by half a year at low latitudes (red color in Fig. 6f, hereafter referred to as Region N3). Nevertheless, further investigation is required to ascertain whether the observed statistical relationship of the six-month lag in Chl-*a* is physically significant. Regions P3 and N3 are not discussed in this study.

The fundamental characteristics of the primary variables, MLD, Chl-*a*, and iron, are examined in the four regions mentioned above. Figure 7 shows the monthly averages of these variables in each region. The error bars indicate the variability or uncertainty in the data. As expected, three variables exhibit significant seasonal variation, with consistent changing trends observed across the different regions. Region P2, situated within the deep MLD band, consistently maintains the deepest MLD among the four regions throughout the year. The Chl-*a* level exhibits minimal discrepancies across the four regions, while the highest concentration of dissolved iron is found in the vicinity of the Antarctic (Region N1).

Therefore, we identify the areas with the most significant positive and negative correlations between MLD and Chl-*a*, as well as the lag response time of Chl-*a*. The primary contribution of MLD deepening is to facilitate the growth of phytoplankton by entraining iron from the subsurface to the surface (Fauchereau et al., 2011; Tagliabue et al., 2014). To further investigate the influence of MLD deepening on the Chl-*a* distribution in these regions, the correlations among MLD, Chl-*a*, and iron are calculated for each season. Figure 8 presents the time series and correlation coefficients of these three variables in Region P1 across different seasons. The response of Chl-*a* to the MLD in Region P1 is instantaneous and occurs at lower latitudes (north of 40°S). The magnitude of Chl-*a* is approximately 0.1 mg/m^3 throughout

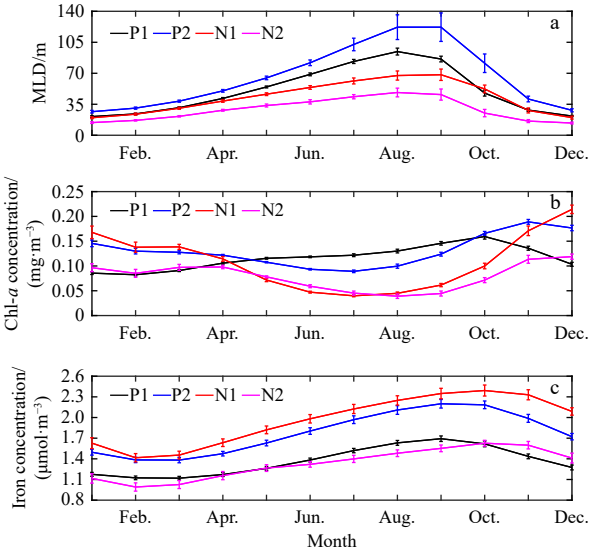

Fig. 7. Time series of MLD (a), Chl-*a* (b), and iron (c) in the selected regions (P1, P2, N1, and N2). The error bars represent the standard deviation.

the year, with a maximum level of 0.15 mg/m^3 observed during the austral spring (Fig. 8a). Meanwhile the peak of Chl-*a* occurs in the austral spring, the entrainment of the MLD works in the austral summer. The correlation coefficient between the MLD and Chl-*a* is 0.79 (p = 0.01), and that between the MLD and iron is 0.66 (p = 0.05) (Fig. 8b). These results indicate that the deepening of the MLD in the austral summer entrains iron from the subsurface to the surface, which promotes the growth of phytoplankton. In addition, a statistically significant negative correlation between the MLD and Chl-*a* emerges in the austral winter (r = –0.74, p = 0.02) (Fig. 8d). As the MLD is deeper than the euphotic layer in the austral winter, the MLD deepening increases light limitation. To further examine the physical processes responsible for the vertical transport of iron during summer, the correlation coefficients of the terms of Eq. (5), MLD, and iron are calculated as shown in Table 1. The correlation coefficient between the entrainment item and iron is 0.84 (p = 0.005), which provides evid-

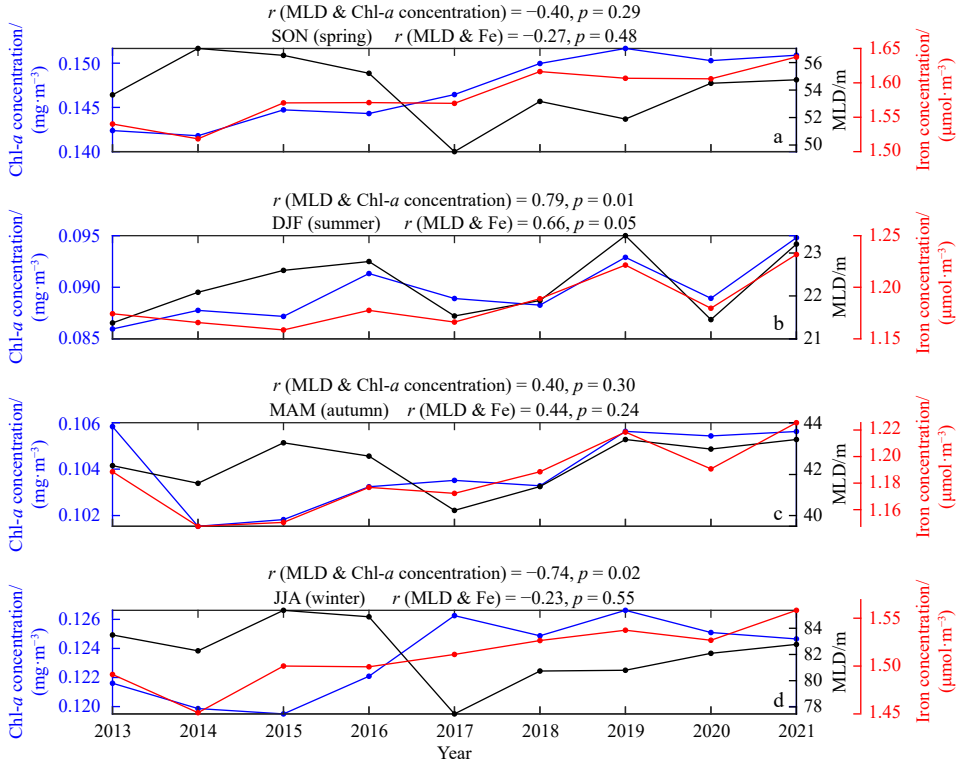

Fig. 8. Time series and connections of MLD, Chl, and iron in annual spring (a), summer (b), autumn (c), and winter (d) in Region P1. The magnitudes are calculated by domain-averaged over Region P1.

Table 1. Correlation coefficients for each term in Eq. (5) and the MLD and iron over Region P1 in summer

	w	$\frac{\partial h}{\partial t}$	w_b	$\boldsymbol{V}\cdot\nabla h$
w	–	–0.07	0.26	0.40
MLD	0.29	–0.53	0.06	0.49
Fe	0.84*	–0.16	0.24	0.39

Note: The asterisk (*) represents that the results are statistically significant at the 95% confidence level. – denotes no data.

ence that the MLD deepening exerts an entrainment effect on iron in summer.

In comparison to Region P1, Region P2 is situated at mid-latitudes, and the influence of the MLD on Chl-*a* is delayed by one season. This means that the entrainment of the MLD operates in the following season. Theoretically, the MLD transports iron to the surface during the austral winter (spring), and phytoplankton utilizes the austral winter (spring) iron stocks to grow when austral spring (summer) light intensifies (Arrigo et al., 2008; Fauchereau et al., 2011). Therefore, we calculate the correlation between MLD and iron with Chl-*a* in the subsequent season, and the correlation between MLD and iron in the same duration as shown in Fig. 9. Taking the austral winter MLD as an example, we calculate the correlation coefficients between austral winter MLD and iron with austral spring Chl-*a*, respectively. Additionally, we calculate correlation coefficients between the austral winter MLD and iron. The entrainment effect of MLD is strongest in spring and winter (Figs 9a and d) with correlation coefficients of 0.95 (p = 0.000 1) and 0.97 (p = 0.000 02), respectively. Although the MLD and iron synergized well in the austral spring and winter, they fail to promote Chl-*a* increase in the subsequent season. The correlation coefficient between austral spring iron and summer Chl-*a* is –0.10 (p = 0.82) and the coefficient between austral winter iron and spring Chl-*a* is –0.30 (p = 0.42). Previous statistical results show that the response of Chl-*a* in Region P3 responds to the MLD with a delay of around six months (Fig. 6c). However, the physical significance of this delay remains uncertain due to its extensive response time.

Region N1 is the region where MLD and Chl-*a* are instantaneously negatively correlated. Figure 10 shows the time series and correlation coefficients of MLD, Chl-*a*, and iron in Region N1 for various seasons. The largest Chl-*a* appears in the austral summer, with values ranging from 0.1 mg/m^3 to 0.2 mg/m^3 (Fig. 10b). The other three seasons are lower than 0.12 mg/m^3 (Figs 10a, c, and d). The MLD and Chl-*a* show a negative correlation throughout the year. Specifically, the correlations for austral spring, summer, autumn, and winter are –0.81 (p = 0.008), –0.24 (p = 0.54), –0.52 (p = 0.15) and –0.93 (p = 0.000 3), respectively. In addition, negative correlations are observed between MLD and iron in all seasons, which contradicts the theory that MLD deepening increases iron input to the surface layer. The MLD is thus not the primary factor driving the increase in Chl-*a*. Considering that Region N1 is covered by sea ice, the melting of this ice contributes to phytoplankton growth as it is an essential source of iron input (Arrigo et al., 2008; Behera et al., 2020). Therefore correlations between SIC, Chl-*a*, and iron are calculated in all seasons. In the austral summer, the correlation coefficient between sea ice and iron is 0.86 (p = 0.003), and the coefficient between sea ice and Chl-*a* is 0.85 (p = 0.004). This indicates that an increase in sea ice melt leads to a higher release of iron in the austral summer, which promotes phytoplankton growth. The above analysis indicates that in Region N1, sea ice has a greater impact on the change in Chl-*a* compared to MLD during summer.

Region N2 is located in the eastern Pacific Ocean and is characterized by a minimal negative correlation between MLD and Chl-*a*. This occurs when the Chl-*a* lags behind the MLD by one

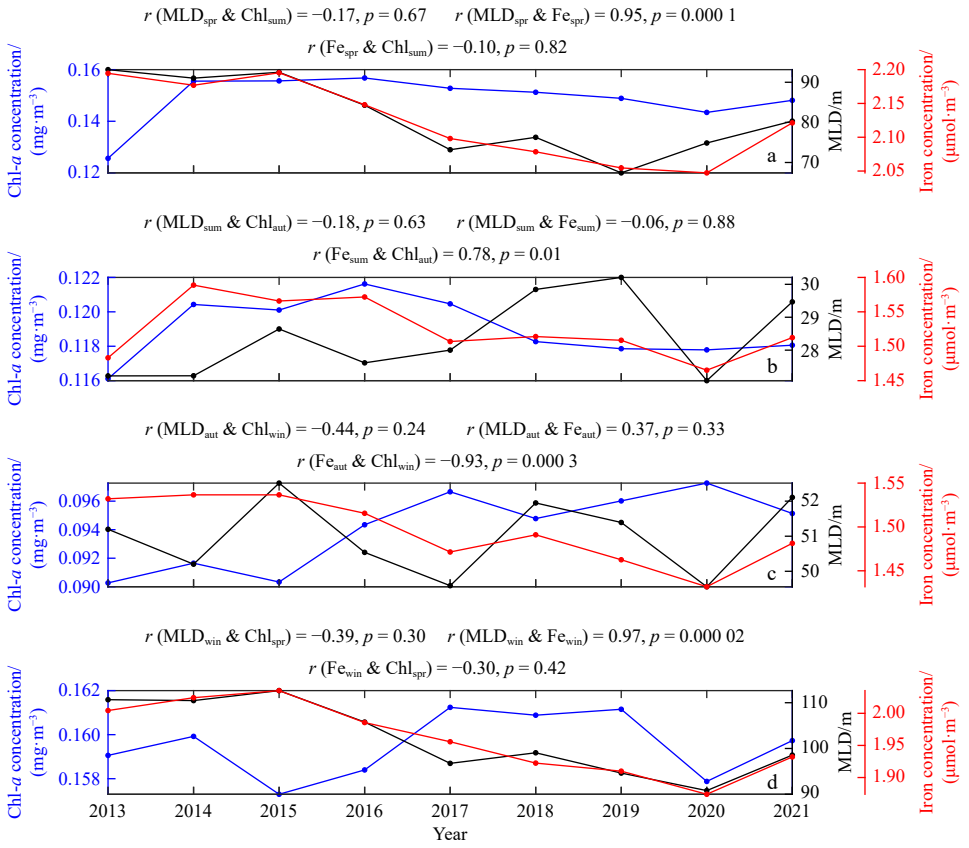

Fig. 9. Time series and connections of MLD, Chl-*a* concentration, and iron in annual spring (a), summer (b), autumn (c), and winter (d) in Region P2. The magnitudes are calculated by domain-averaged over Region P2.

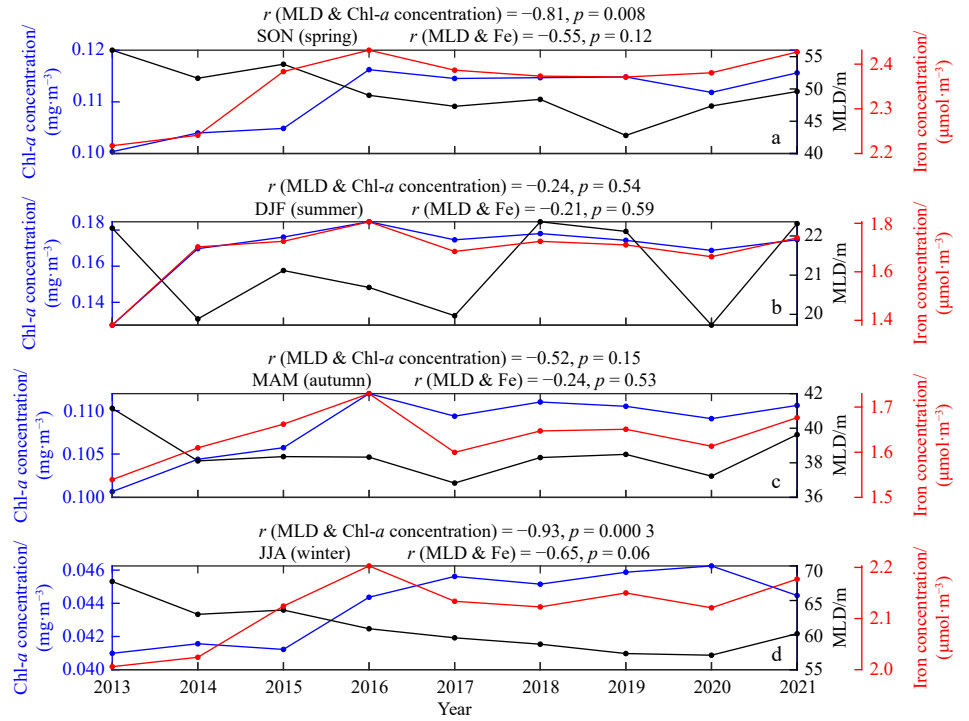

Fig. 10. Time series and connections of MLD, Chl-*a* concentration, and iron in annual spring (a), summer (b), autumn (c), and winter (d) in Region N1. The magnitudes are calculated by domain-averaged over Region N1.

season. In the austral autumn, MLD and Chl-*a* exhibit a positive correlation (Fig. 11c) due to the dilution effect of MLD deepening. This effect results in a reduction in the phytoplankton loss rate to a level below the growth rate, which eventually results in MLD deepening with an increase in Chl-*a* (Behrenfeld et al., 2013). In addition, MLD and iron show a negative correlation (r = –0.69, p = 0.04) during the austral winter (Fig. 11d). This indicates that MLD entrainment does not supplement iron that stimulates the growth of Chl-*a*. Region N2 is located near the west coast of South America, which has been identified as a significant source of iron (Fauchereau et al., 2011). Thus Chl-*a* distribution in Region N2 is closely associated with near-shore iron sources. No significant correlation is found between the MLD and Chl-*a* during the other seasons.

In summary, on the seasonal time scale, the SO can be divided into three positively correlated regions and three negatively correlated regions according to the correlation between the MLD and Chl-*a*. In the subtropical region north of 40°S (Region P1), MLD and Chl-*a* show an instantaneous positive correlation in the austral summer. The deepening of the MLD promotes Chl-*a* increase by increasing iron input. For Region P2, where Chl-*a* lags behind the MLD by one season, although the deepening of the MLD in the austral spring and winter carry more iron to the surface (strongly positively correlated), they do not seem to affect the Chl-*a* increase in the subsequent season. In Region N1 at mid and high latitudes, sea ice rather than the MLD plays a role in the distribution of Chl-*a* during the austral summer. In addition, iron responsible for promoting the Chl-*a* increase in the eastern Pacific Ocean is not derived from the MLD entrainment, but from the nearshore iron source. The response time of Chl-*a* to MLD in Regions P3 and N3 is too long and may not hold physical significance. It is worth noting that the correlation between iron, MLD, and Chl-*a* in some areas is not statistically significant. This implies that other physical processes contribute to phytoplankton growth through increased iron inputs. These processes include vertical diapycnal diffusion, Ekman upwelling, mesoscale eddies, and fronts (He et al., 2016; Tagliabue et al., 2014; Taylor and Ferrari, 2011). The mechanisms in these regions with insignificant correlations are also important and should be investigated in future studies.

5 Relationship between MLD and Chl-*a* on the interannual timescale

Similar to the seasonal variation, the influence of the MLD on Chl-*a* in the interannual variation could be instantaneous or lagged. To identify the seasons in which the MLD affects Chl-*a* on interannual variability, correlations between the MLD and Chl-*a* anomalies are calculated separately for each season. A total of four significant figures are selected from the original sixteen, as illustrated in Fig. 12. Figures 12a and b show that the MLD and Chl-*a* anomalies exhibit a negative correlation in the austral winter and spring due to light limitation, which has been extensively documented (Li et al., 2021). In addition, a positive correlation can be observed between the austral summer MLD anomaly and the summer Chl-*a* anomaly, as well as between the austral winter MLD anomaly and the spring Chl-*a* anomaly. These findings indicate that the deepening of the MLD promotes Chl-*a* development, which will be further explored in this study (Figs 12c and d).

The low Chl-*a* in the SO results from iron limitation, which

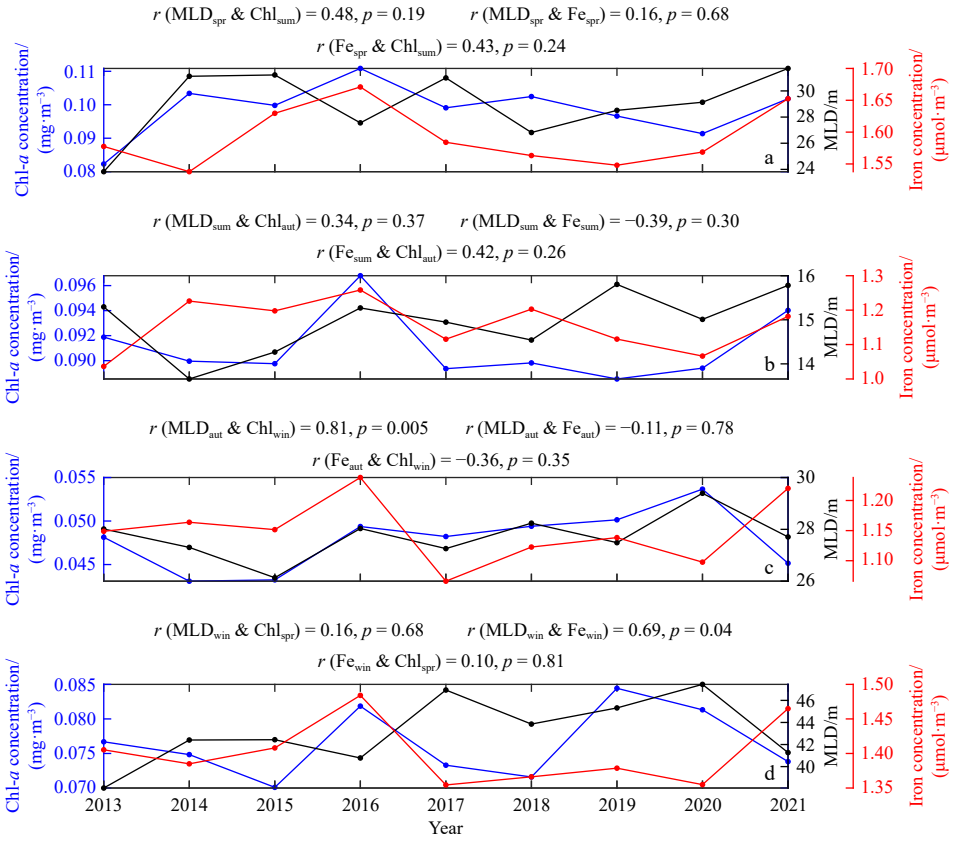

Fig. 11. Time series and connections of MLD, Chl-*a* concentration, and iron in annual spring (a), summer (b), autumn (c), and winter (d) in Region N2. The magnitudes are calculated by domain-averaged over Region N2.

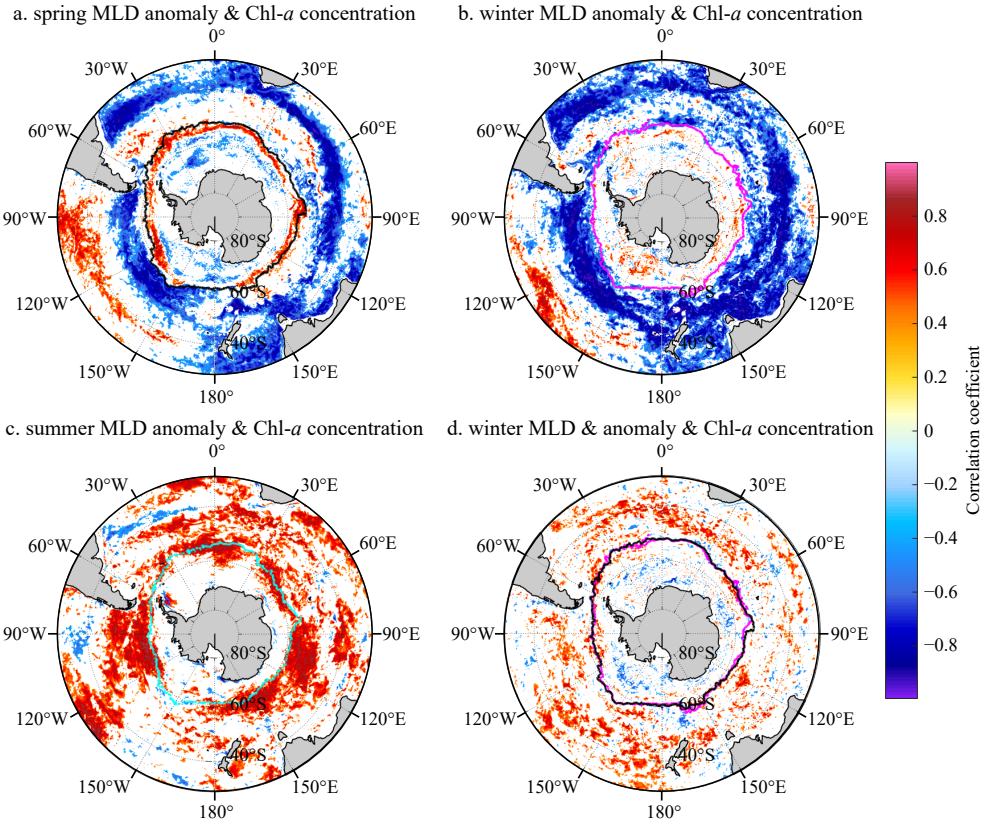

Fig. 12. Correlation coefficients between MLD anomaly and Chl-*a* anomaly in the austral spring (a), summer (b), autumn (c), and winter (d) MLD and spring Chl-*a*. The black, cyan, and pink contours represent the edges of sea ice in the austral spring, summer, and winter, respectively. White regions represent correlations with $p > 0.05$.

has been well demonstrated (Boyd et al., 1999; Fauchereau et al., 2011). Figure 13a shows the correlation coefficient between Chl-*a* and iron anomalies during the austral summer. On the one hand, the Chl-*a* and iron anomalies exhibit a strong positive correlation south of 40°S, which is consistent with previous studies (Arrigo et al., 2008; Boyd, 2002; Fauchereau et al., 2011). On the other hand, the MLD and Chl-*a* anomalies show a positive correlation in the austral summer (Fig. 12c), indicating that a deeper MLD favors Chl-*a* increase. However, this finding alone does not confirm that the increase in Chl-*a* is directly resulting from the increased iron input due to the entrainment effect of the MLD. Therefore, the relationship between MLD and iron anomalies is further investigated, as shown in Fig. 13b. The results show a strong positive correlation between the two variables, with a noticeable occurrence within the 40°–60°S deep MLD zone. This finding suggests that a deeper MLD promotes the input of iron to the surface, ultimately affecting Chl-*a* increase.

By combining Figs 12c and 13b, we can identify the regions where Chl-*a* distribution is influenced by the austral summer MLD through the entrainment of iron. These regions are mainly located in the deep MLD band, as shown in Fig. 14a. Notably, except for the deep MLD band at mid-latitudes, Chl-*a* distribution around Antarctica and at lower latitudes is not modulated by the MLD. To find out the physical factors controlling Chl-*a* increase

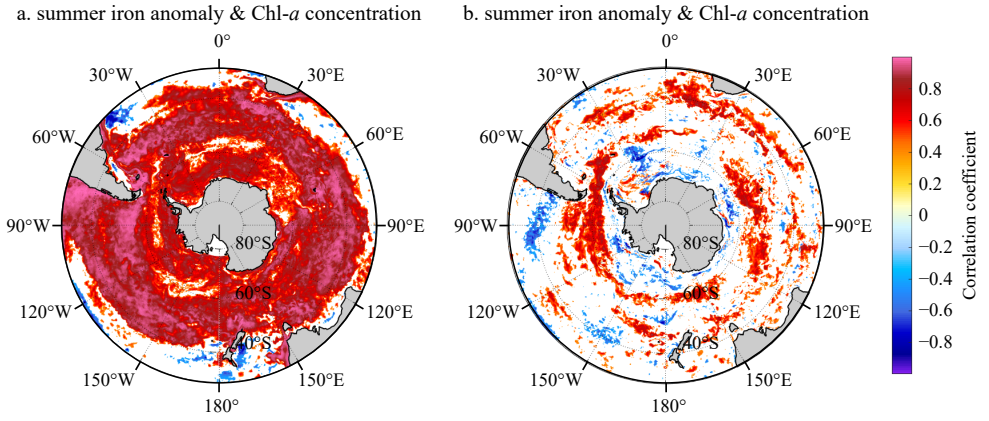

Fig. 13. Correlation coefficients between anomaly of iron and Chl-*a* (a), MLD (b) in the austral summer. White regions represent correlations with $p > 0.05$.

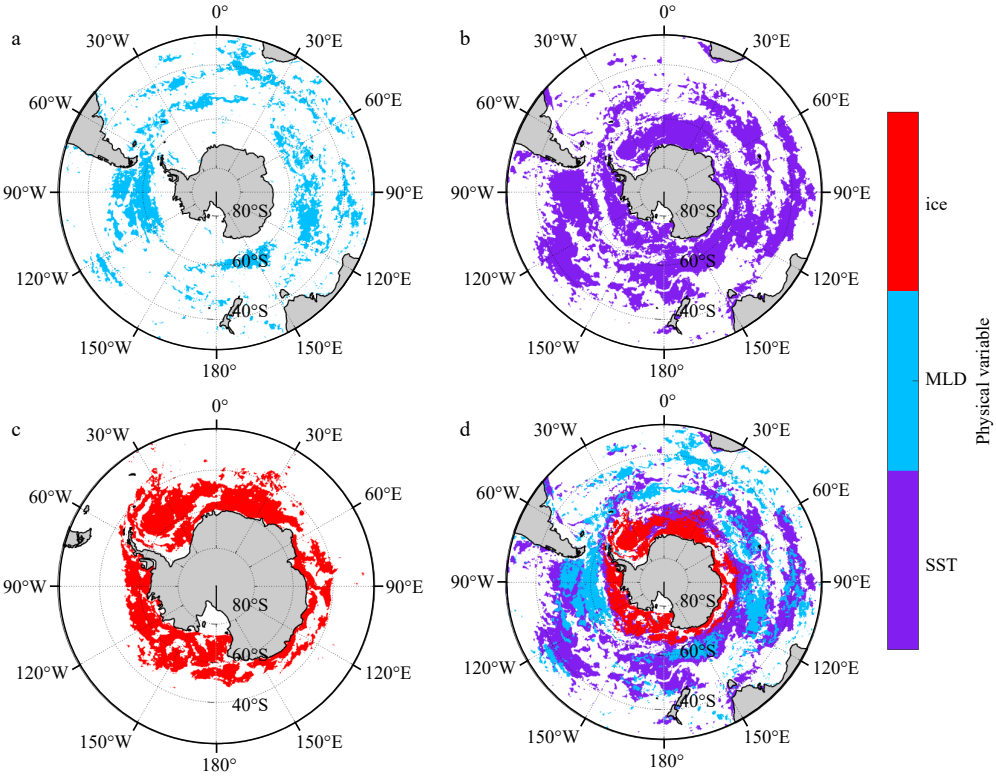

Fig. 14. A schematic summarizing the response of Chl-*a* anomaly to the physical variables in the austral summer. The regions in blue, purple, and red indicate the areas where the influence of austral summer MLD, SST, and sea ice is significant, respectively.

in these remaining regions, the relationships of SST anomaly to Chl-*a* and iron anomalies in the austral summer are calculated, respectively. The results show that SST anomaly is strongly negatively correlated to Chl-*a* and iron anomalies, suggesting that sea surface cooling facilitates iron transport to the surface layer and thus promotes Chl-*a* increase. Figure 14b shows the regions in the SO that simultaneously satisfy the negative association of SST anomaly to iron and Chl-*a* anomalies. Compared to Fig. 14a, the regions where the SST works are larger than those where MLD works. Since the MLD variation itself is accompanied by SST variation, an overlapping region appears. Changes in SST in other places may be influenced by other physical processes such as upwelling, which affect the distribution of Chl-*a* (Aguirre et al., 2018). Similarly, the same approach is used to identify areas where sea ice works, as shown in Fig. 14c. These areas represent the positive association with SIC anomaly to iron and Chl-*a* anomalies. This indicates that sea ice melting in the austral summer encourages iron input and thus phytoplankton blooms.

Accordingly, in conjunction with Figs 14a–c, a schematic of the physical processes governing the summer Chl-*a* distribution on the interannual time scale can be obtained (Fig. 14d). One can see that south of 60°S, the Chl-*a* distribution is dominated by sea ice melting, while north of 60°S, SST and MLD are the main factors. It is worth noting that the MLD and SST overlap in the Pacific and Indian Oceans, and the overlapping regions coincide with the deep MLD band (40°S–60°S). The MLD concurrently impacts SST, and the combined effect of both factors controls the distribution of Chl-*a*. To better examine the physical mechanism in the MLD-dominated region, domain-averaged terms in Eq. (5) and iron as well as their correlation coefficients are calculated during annual summer (Fig. 15). Iron is strongly correlated with the entrainment ($r = 0.75$, $p = 0.02$) and the horizontal advection term ($r = 0.70$, $p = 0.04$). However, entrainment is not strongly correlated with other terms. Furthermore, correlation coefficients between the MLD and Eq. (5) are also calculated. The MLD shows a strong positive correlation with entrainment ($r = 0.87$, $p = 0.02$) and the horizontal advection term ($r = 0.83$, $p = 0.006$). This suggests that horizontal advection-induced entrainment is a major factor inducing iron input in summer on the interannual time scale.

Previous studies have confirmed that the austral winter MLD stimulates spring productivity, but only on the seasonal time scale. As shown in Figs 12d and 16a, on the interannual time scale, the austral winter MLD increases surface iron supply, which affects the distribution of Chl-*a* in the subsequent season. The positive correlation between the austral winter MLD and iron anomalies also supports the concept that the entrainment of the MLD deepening transports iron to the surface layer (Fig. 16b). This finding is at odds with previous research that failed to observe an impact of austral winter MLD on spring productivity at the interannual time scale (Li et al., 2021).

By combining Figs 12d and 16b, the area where the austral winter MLD entrains iron and affects the austral subsequent spring Chl-*a* distribution can be obtained, as shown in Fig. 17a. The affected area is primarily located north of 60°S. During the austral winter, the area south of 60°S is covered by ice, so the correlations between winter SIC anomaly relative to austral winter iron and spring Chl-*a* anomaly are calculated. The correlation coefficient between the austral winter SIC and the iron anomaly is not significantly related south of 60°S due to the patchy distribution of the correlation coefficient. The austral winter SIC and the spring Chl-*a* anomaly are negatively correlated only near the Amundsen and the Cosmonaut seas. Combining the relationship of SIC, Chl-*a*, and iron anomaly, the area where austral winter

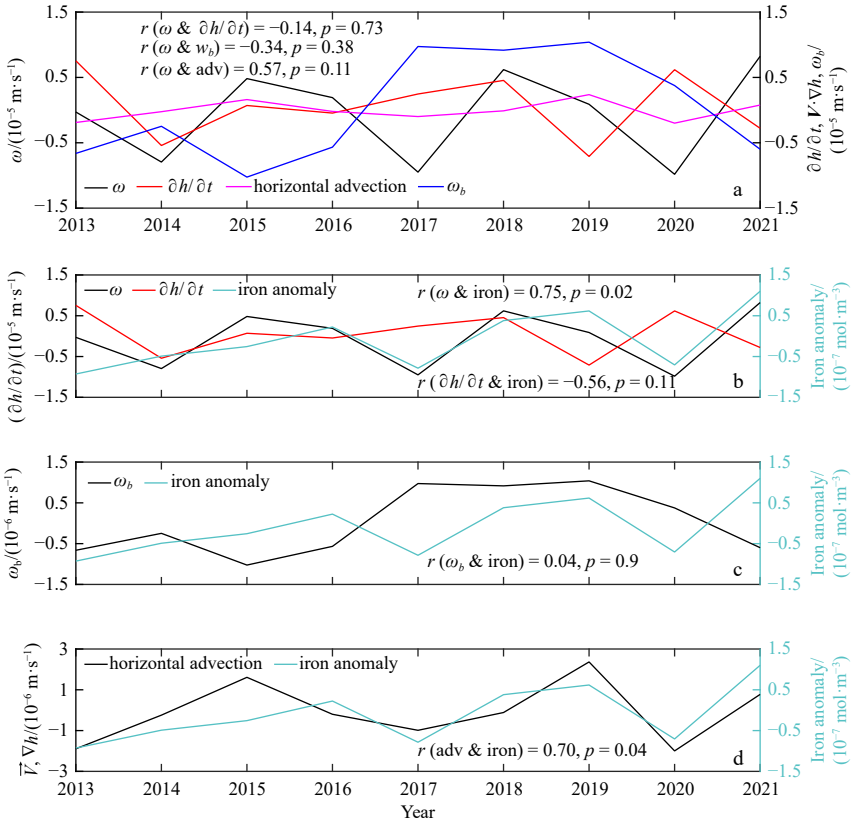

Fig. 15. Time series and connections of the three terms in Eq. (5) [$\partial h/\partial t$, the rate of MLD deepening; w_b, the vertical velocity at the ML base; $\vec{V}\cdot\nabla h$, the horizontal advection (adv) of water in the ML] and iron anomalies in annual summer. The magnitudes are calculated by domain-averaged over Fig. 14a, where the MLD works in the austral summer.

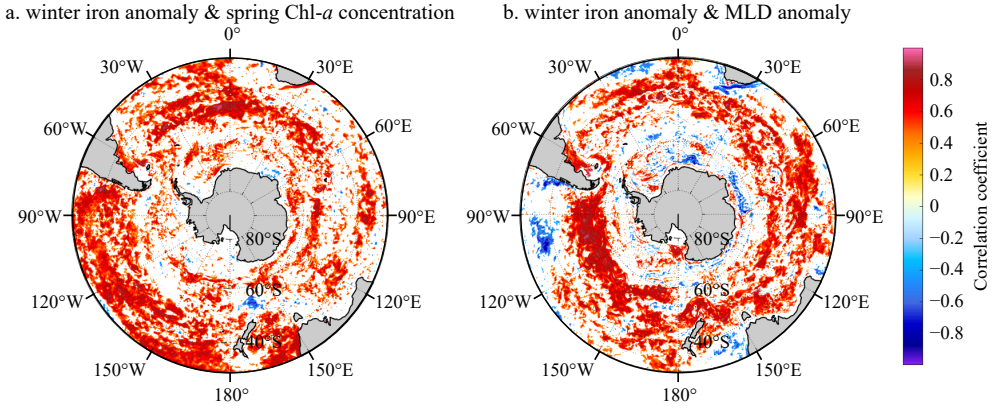

Fig. 16. Correlation coefficients of winter iron anomaly and spring Chl-*a* (a) and winter MLD (b). White regions represent correlations with $p > 0.05$.

SIC controls Chl-*a* by affecting iron input can be obtained, as shown in Fig. 17c. The contribution of SIC to the entire SO region is minimal and negligible. Moreover, our analysis of the correlation between winter SST and iron, as well as that between the austral winter SST and spring Chl-*a* anomaly, reveals that the austral winter SST anomaly is negatively correlated with austral winter iron and spring Chl-*a* anomaly, respectively. This indicates that winter sea surface cooling favors iron input and spring Chl-*a* increases. The area where SST plays a role is shown in Fig. 17b.

Based on Figs 17a–c, Fig. 17d depicts the regions where winter MLD, SST, and SIC influence spring Chl-*a* distribution in the SO. In contrast to the results in the austral summer (Fig. 14d), SIC seems to have little effect near Antarctica. Furthermore, the effective domains of MLD and SST are also reduced, respectively. Overlapping areas are observed only in the central Pacific. Since this section mainly focuses on the influence of physical processes related to the MLD on the iron input and subsequently the Chl-*a* distribution, we select areas where the MLD has a notable effect for further analysis (Fig. 17a). Figure 18 shows the time series of each term in Eq. (5) and iron in annual winter. The entrainment term and MLD variation term exhibit a strong positive correlation ($r = 0.96$, $p = 0.000\,1$), while the entrainment term is not significantly correlated with the vertical velocity and hori-

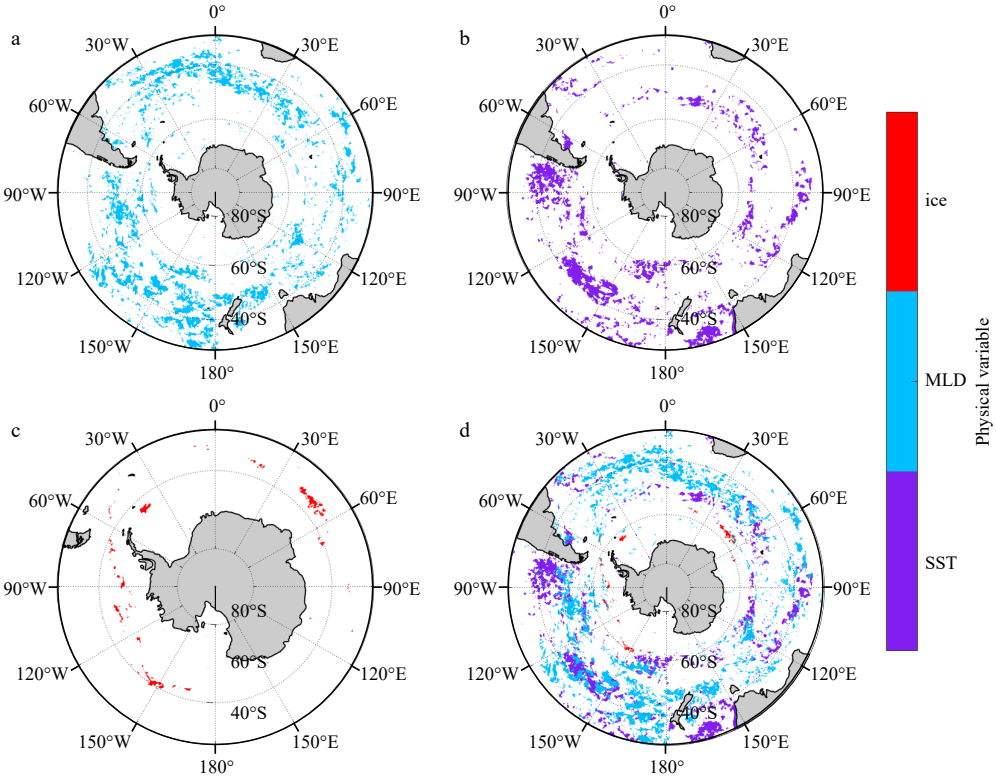

Fig. 17. A schematic summarizing the response of austral spring Chl-*a* anomaly to the physical variables in the austral winter. The regions in blue, purple, and red indicate the areas where austral winter MLD, SST, and sea ice influence are significant, respectively.

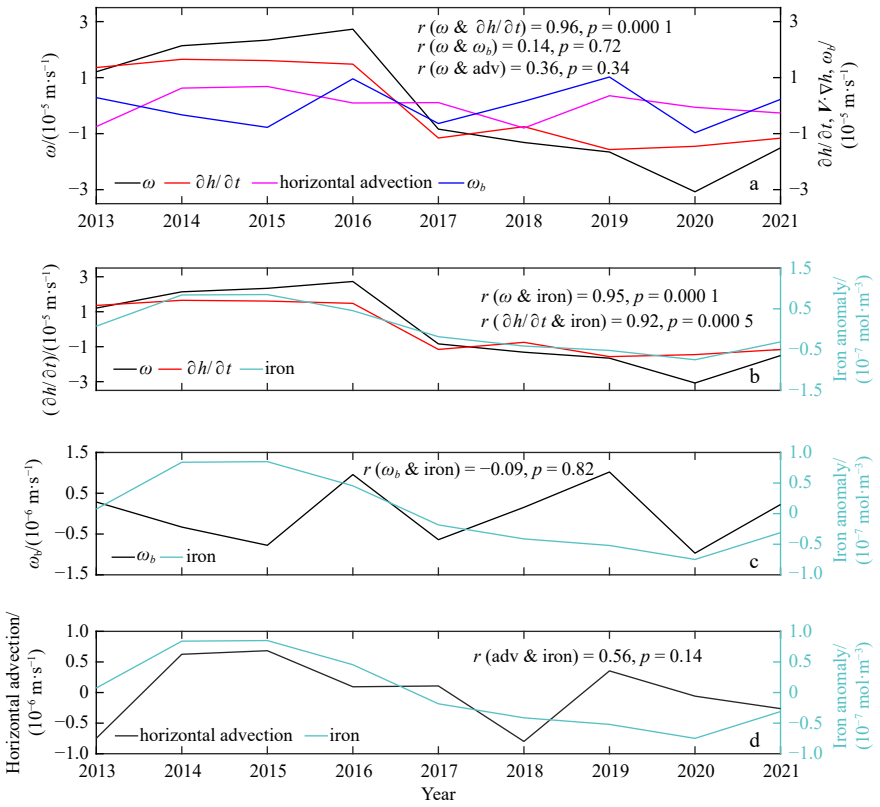

Fig. 18. Time series and connections of three terms in Eq. (5) ($\partial h/\partial t$, the rate of MLD deepening; w_b, the vertical velocity at the ML base; $\boldsymbol{V}\cdot\nabla h$, the horizontal advection (adv) of water in the ML) and iron in annual winter. The magnitudes are calculated by domain-averaged over Fig. 17a, where the MLD works in winter.

zontal advection term (Fig. 18a). In addition, iron is significantly and positively correlated with the entrainment term (r = 0.95, p = 0.000 1) and the MLD variation term (r = 0.92, p = 0.000 5), while there is no significant relationship with the vertical velocity and horizontal term. The MLD also shows a strong positive correlation with the entrainment term (r = 0.94, p = 0.000 2) and the MLD tendency (r = 0.98, p < 0.000 1). The above features suggest that, on the interannual time scale, the entrainment caused by MLD deepening during the austral winter promotes the surface iron stock. Once the limitation of light in the subsequent spring is alleviated, Chl-*a* then utilizes this iron stock. Vertical velocity and horizontal advection effects on iron input can be almost negligible.

6 Conclusions and discussion

Using B-SOSE data during 2013–2021, this study investigates the impact of a deepening MLD on the seasonal and interannual distribution of Chl-*a* in the SO. On the seasonal time scale, the response time of Chl-*a* to the MLD varies with the latitude. In the subtropical region north of 40°S, Chl-*a* has an instantaneous response to the MLD, and the two variables show a positive correlation (Fig. 19a, Region P1). The analysis of the correlations of MLD, Chl-*a*, and iron in each season indicates that the deepening of the MLD in the austral summer brings more iron from the subsurface to the surface, thereby promoting an increase in Chl-*a*. However, in non-summer seasons, no obvious relationship exists between the three. Between 40°S and 60°S, the MLD has a strong positive correlation with Chl-*a* in the subsequent season (Fig. 19a, Region P2). Further analysis of Region P2 reveals that although deepening of the MLD significantly contributes to iron replenishment during the austral spring and winter, it does not promote Chl-*a* increase in the subsequent seasons. Additionally, the summer and autumn MLD has no impact on iron or subsequent seasons' Chl-*a*. According to statistical analysis, the impact of MLD on Chl-*a* is observed six months later in the high-latitude region beneath sea ice cover (Region P3). However, the six-month lagged response time of Chl-*a* may not be of physical significance.

Similarly, in the negative correlation regime between the MLD and Chl-*a*, the time when the MLD acts on Chl-*a* also varies with the latitude. Under sea ice cover (Fig. 19b, Region N1), the impact of the MLD on Chl-*a* is instantaneous. The analysis of different seasons in the Region N1 shows a negative correlation in the austral spring and winter, indicating that MLD deepening limits the availability of light for phytoplankton. the primary factor influencing the distribution of Chl-*a* is the melting of sea ice. The region where Chl-*a* lags behind the MLD by one season is located in the East Pacific (Fig. 19b, Region N2). A year-long analysis of relationships of the MLD, Chl-*a*, and iron shows that during the austral autumn, the MLD deepens and dilutes the

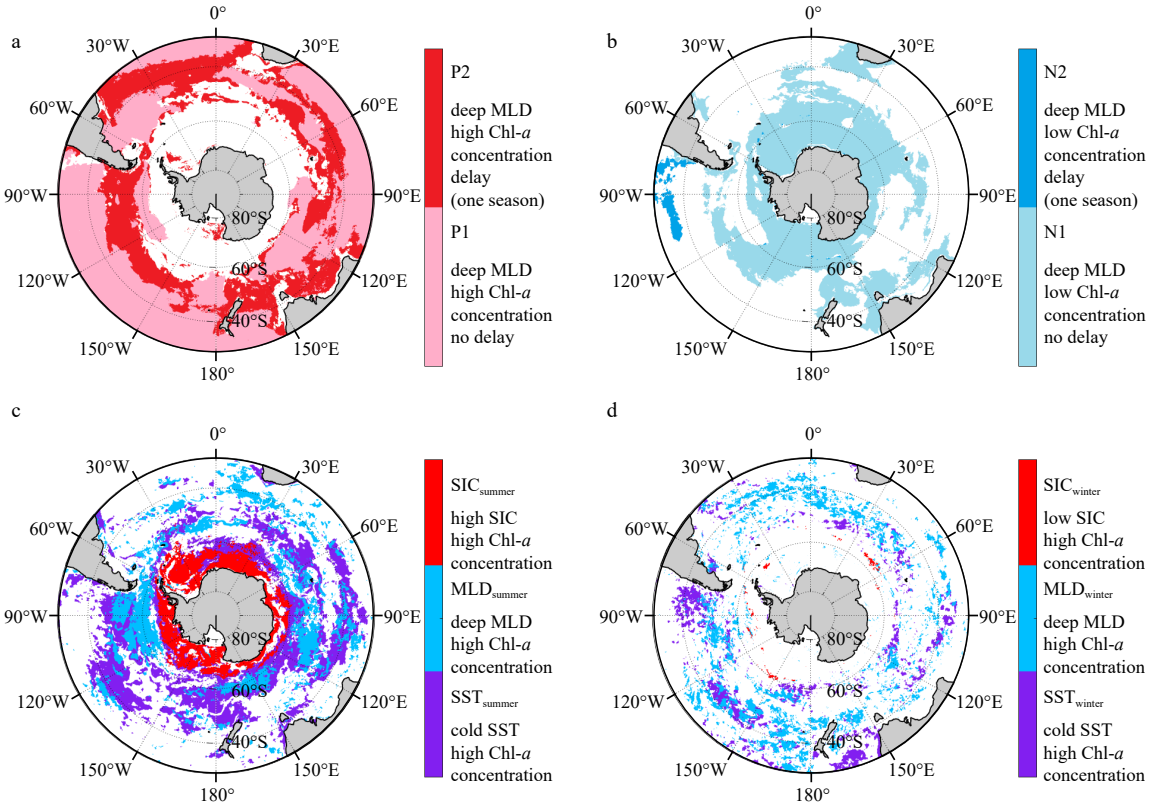

Fig. 19. A schematic summarizing the response of phytoplankton biomass to various primary physical variables in the SO on seasonal (a, b) and interannual (c, d) time scales. a. Positively correlated regions, regions in pink (P1) and red (P2) represent regions of deep MLD with high Chl-*a* (positively correlated). b. Negatively correlated regions, regions in light blue (N1) and blue (N2) represent regions of deep MLD with low Chl-*a* (negatively correlated). Regions P1 and N1 exhibit synchronous responses of Chl-*a* to the MLD, while Regions P2 and N2 show a one-season lagged responses of Chl-*a* to the MLD. c. Synchronous influence regions, regions showing positive anomalies in summer Chl-*a* are associated with negative anomalies in summer SST (purple), positive anomalies in summer MLD (blue), and positive anomalies in summer SIC (red). d. Delayed influence regions, regions showing positive anomalies in spring Chl-*a* are associated with negative anomalies in winter SST (purple), positive anomalies in winter MLD (blue), and negative anomalies in winter SIC (red).

herbivore population, causing a decrease in the Chl-*a* loss rate, which is lower than the Chl-*a* splitting rate. Consequently, there is an increase in Chl-*a*. The case of Region N3 in the subtropics is similar to Region P3.

For the interannual variability, the regions where the MLD impact on Chl-*a* are mainly concentrated between 40°S and 60°S during the austral summer and winter (regions in blue of Figs 19c and d). The influence of the MLD on Chl-*a* is primarily reflected in entrainment, whereby MLD deepening increases surface iron input. In the austral summer, entrainment due to horizontal advection contributes to iron input between 40°–60°S (the region in blue of Fig. 19c). In the south of 60°S, sea ice melting is the main factor of Chl-*a* distribution (the region in red of Fig. 19c). In addition, changes in SST have an impact on Chl-*a* change (the region in purple of Fig. 19c). In addition to the synchronous influences of summer MLD and other variables on Chl-*a* mentioned above, there are also lagged impacts in specific regions, characterized by the influence of the winter MLD on subsequent spring Chl-*a*. During the austral winter, the MLD deepening increases iron stock and promotes subsequent spring Chl-*a* increase in the SO (the region in blue of Fig. 19d). It should be noted that the austral winter sea ice in the austral region does not contribute to Chl-*a* increase in the austral spring, as we can barely find areas where the two are highly correlated (the region in red of Fig. 19d). However, the winter SST is still a factor affecting spring Chl-*a* in the SO, and possible mechanisms need further investigation (the region in purple of Fig. 19d).

Although this study effectively reveals the regions and mechanisms for the SO MLD deepening to affect phytoplankton using B-SOSE data, it is important to point out its limitations. Specifically, this study fails to consider mesoscale and submesoscale dynamical processes. Moreover, the resolution of the B-SOSE data is (1/6)°, which may not adequately capture some mesoscale and submesoscale physical and biochemical processes. Previous studies have indicated that these processes have a significant impact on MLD variability and the iron input, and thus cannot be ignored. These include mesoscale eddies and upwelling (He et al., 2016; Medina-Gómez et al., 2019; Taylor and Ferrari, 2011). Furthermore, the relatively brief 9-year temporal coverage of B-SOSE data somewhat restricts the analysis on longer time scales. In addition to the limitations in spatial and temporal resolution, as products of model output, B-SOSE data is also constrained by model assumptions, the lack of observational data, and internal uncertainties within the model, such as model structure and parameterization schemes. All of these factors may lead to limitations in the data and may erroneously affect statistical results. However, these limitations are not deemed critical, thus ensuring the reliability and robustness of the primary conclusions presented in this paper. Future studies should address these limitations to strengthen the robustness of the conclusions.

This study is based on the assumption of HNLC (Arrigo et al., 2008; Boyd et al., 1999; Boyd, 2002), thus the influence of nutrients on the Chl-*a* distribution is not considered. However, the spatiotemporal distribution characteristics of nutrients in the SO may be scarce at certain times or regions, thus affecting phytoplankton growth. This study solely focuses on the impact of iron sources on Chl-*a*, as iron proves crucial in the SO's Chl-*a* development. This study investigates iron inputs induced by MLD entrainment but does not consider the specific sources of iron. In addition to winter deep mixing, iron input into the ocean can also occur via vertical diapycnal diffusion and Ekman upwelling/downwelling (De Baar et al., 1995; Moore et al., 2001; Tagliabue et al., 2014). The iron input due to entrainment is approximately ten times greater than the Ekman upwelling/downwelling, with an average annual flux of 20×10^6 mol/(m^2·a) for Fe. However, the contribution of vertical diapycnal diffusion is minimal, with a yearly average flux of -1×10^6 mol/(m^2·a) for Fe (Tagliabue et al., 2014). The iron flux in the B-SOSE model considers all potential iron sources, such as atmospheric dust deposition, sea ice melting, river runoff, sediment removal, and remineralization (Galbraith et al., 2010; Verdy and Mazloff, 2017). River runoff and sea/glacial ice melting are considered as local inputs (Behera et al., 2020; Smith and Comiso, 2008). Iron inputs due to these processes may also reach a maximum of 20×10^6 mol/(m^2·a) for Fe, which is equal to that from entrainment (Boyd et al., 2012). Nevertheless, the maximum value is only observed in iron-replete source areas, such as nearshore waters and regions adjacent to sea ice. These processes play a pivotal role in the local supply of surface iron and are indispensable in local studies. However, ML entrainment is important throughout the SO. Therefore, further research on the influence of iron sources and nutrients on the distribution of Chl-*a* in the SO is crucial, as it has the potential to impact primary productivity and climate change.

Acknowledgement

Hailong Liu would like to acknowledge support from the ICTP through the Associates Programme (2020–2025).

References

Aguirre C, García-Loyola S, Testa G, et al. 2018. Insight into anthropogenic forcing on coastal upwelling off south-central Chile. Elementa: Science of the Anthropocene, 6: 59, doi: 10.1525/elementa.314

Arrigo K R, Van Dijken G L. 2003. Phytoplankton dynamics within 37 Antarctic coastal polynya systems. Journal of Geophysical Research: Oceans, 108(C8): 3271, doi: 10.1029/2002jc001739

Arrigo K R, Van Dijken G L, Bushinsky S. 2008. Primary production in the Southern Ocean, 1997–2006. Journal of Geophysical Research: Oceans, 113(C8): C08004, doi: 10.1029/2007jc004551

Behera N, Swain D, Sil S. 2020. Effect of Antarctic sea ice on chlorophyll concentration in the Southern Ocean. Deep-Sea Research Part II: Topical Studies in Oceanography, 178: 104853, doi: 10.1016/j.dsr2.2020.104853

Behrenfeld M J, Doney S C, Lima I, et al. 2013. Annual cycles of ecological disturbance and recovery underlying the subarctic Atlantic spring plankton bloom. Global Biogeochemical Cycles, 27(2): 526–540, doi: 10.1002/gbc.20050

Blain S, Quéguiner B, Armand L, et al. 2007. Effect of natural iron fertilization on carbon sequestration in the Southern Ocean. Nature, 446(7139): 1070–1074, doi: 10.1038/nature05700

Bowie A R, Van Der Merwe P, Quéroué F, et al. 2015. Iron budgets for three distinct biogeochemical sites around the Kerguelen Archipelago (Southern Ocean) during the natural fertilisation study, KEOPS-2. Biogeosciences, 12(14): 4421–4445, doi: 10.5194/bg-12-4421-2015

Boyd P W. 2002. Environmental factors controlling phytoplankton processes in the Southern Ocean. Journal of Phycology, 38(5): 844–861, doi: 10.1046/j.1529-8817.2002.t01-1-01203.x

Boyd P W, Arrigo K R, Strzepek R, et al. 2012. Mapping phytoplankton iron utilization: insights into Southern Ocean supply mechanisms. Journal of Geophysical Research: Oceans, 117(C6): C06009, doi: 10.1029/2011jc007726

Boyer T P, Baranova O K, Coleman C, et al. 2019. World ocean database 2018. Silver Spring: U.S. Department of Commerce

Boyd P W, Ellwood M J. 2010. The biogeochemical cycle of iron in the ocean. Nature Geoscience, 3(10): 675–682, doi: 10.1038/ngeo964

Boyd P, Laroche J, Gall M, et al. 1999. Role of iron, light, and silicate in controlling algal biomass in subantarctic waters SE of New Zealand. Journal of Geophysical Research: Oceans, 104(C6): 13395–13408, doi: 10.1029/1999jc900009

Boyd P W, Watson A J, Law C S, et al. 2000. A mesoscale phytoplank-

ton bloom in the polar Southern Ocean stimulated by iron fertilization. Nature, 407(6805): 695–702, doi: 10.1038/35037500
Carranza M M, Gille S T. 2015. Southern Ocean wind-driven entrainment enhances satellite chlorophyll-*a* through the summer. Journal of Geophysical Research: Oceans, 120(1): 304–323, doi: 10.1002/2014jc010203
Carton J A, Grodsky S A, Liu Hailong. 2008. Variability of the oceanic mixed layer, 1960–2004. Journal of Climate, 21(5): 1029–1047, doi: 10.1175/2007jcli1798.1
Chu P C. 1993. Generation of low-frequency unstable modes in a coupled equatorial troposphere and ocean mixed-layer model. Journal of the Atmospheric Sciences, 50(5): 731–749, doi: 10.1175/1520-0469(1993)0502.0.CO;2
Chu P C, Garwood R W Jr. 1991. On the two-phase thermodynamics of the coupled cloud-ocean mixed layer. Journal of Geophysical Research: Oceans, 96(S01): 3425–3436, doi: 10.1029/90JC01862
Chu P C, Garwood R W Jr, Muller P. 1990. Unstable and damped modes in coupled ocean mixed layer and cloud models. Journal of Marine Systems, 1(1/2): 1–11, doi: 10.1016/0924-7963(90)90051-B
De Baar H J W, De Jong J T M, Bakker D C E, et al. 1995. Importance of iron for plankton blooms and carbon dioxide drawdown in the Southern Ocean. Nature, 373(6513): 412–415, doi: 10.1038/373412a0
De Boyer Montégut C, Madec G, Fischer A S, et al. 2004. Mixed layer depth over the global ocean: an examination of profile data and a profile-based climatology. Journal of Geophysical Research: Oceans, 109(C12): C12003, doi: 10.1029/2004jc002378
Dong Shenfu, Sprintall J, Gille S T, et al. 2008. Southern Ocean mixed-layer depth from argo float profiles. Journal of Geophysical Research: Oceans, 113(C6): C06013, doi: 10.1029/2006jc004051
Fauchereau N, Tagliabue A, Bopp L, et al. 2011. The response of phytoplankton biomass to transient mixing events in the Southern Ocean. Geophysical Research Letters, 38(17): L17601, doi: 10.1029/2011gl048498
Frants M, Gille S T, Hatta M, et al. 2013. Analysis of horizontal and vertical processes contributing to natural iron supply in the mixed layer in southern Drake Passage. Deep Sea Research Part II: Topical Studies in Oceanography, 90: 68–76, doi: 10.1016/j.dsr2.2012.06.001
Galbraith E D, Gnanadesikan A, Dunne J P, et al. 2010. Regional impacts of iron-light colimitation in a global biogeochemical model. Biogeosciences, 7(3): 1043–1064, doi: 10.5194/bg-7-1043-2010
Geibert W, Assmy P, Bakker D C E, et al. 2010. High productivity in an ice melting hot spot at the eastern boundary of the Weddell Gyre. Global Biogeochemical Cycles, 24(3): GB3007, doi: 10.1029/2009GB003657
Graham R M, De Boer A M, Van Sebille E, et al. 2015. Inferring source regions and supply mechanisms of iron in the Southern Ocean from satellite chlorophyll data. Deep-Sea Research Part I: Oceanographic Research Papers, 104: 9–25, doi: 10.1016/j.dsr.2015.05.007
He Qingyou, Zhan Haigang, Cai Shuqun, et al. 2016. Eddy effects on surface chlorophyll in the northern South China Sea: mechanism investigation and temporal variability analysis. Deep Sea Research Part I: Oceanographic Research Papers, 112: 25–36, doi: 10.1016/j.dsr.2016.03.004
Helber R W, Kara A B, Richman J G, et al. 2012. Temperature versus salinity gradients below the ocean mixed layer. Journal of Geophysical Research: Oceans, 117(C5): C05006, doi: 10.1029/2011jc007382
Hense I, Bathmann U V, Timmermann R. 2000. Plankton dynamics in frontal systems of the Southern Ocean. Journal of Marine Systems, 27(1–3): 235–252, doi: 10.1016/S0924-7963(00)00070-1
Korb R E, Whitehouse M J, Atkinson A, et al. 2008. Magnitude and maintenance of the phytoplankton bloom at South Georgia: a naturally iron-replete environment. Marine Ecology Progress Series, 368: 75–91, doi: 10.3354/meps07525
Lancelot C, De Montety A, Goosse H, et al. 2009. Spatial distribution of the iron supply to phytoplankton in the Southern Ocean: a model study. Biogeosciences, 6(12): 2861–2878, doi: 10.5194/bg-6-2861-2009
Li Zuchuan, Lozier M S, Cassar N. 2021. Linking Southern Ocean mixed-layer dynamics to net community production on various timescales. Journal of Geophysical Research: Oceans, 126(10): e2021JC017537, doi: 10.1029/2021jc017537
Ma Jinfeng, Liu Hailong, Lin Pengfei, et al. 2021. Effects of the seasonal variation in chlorophyll concentration on sea surface temperature in the global ocean. Acta Oceanologica Sinica, 40(11): 50–61, doi: 10.1007/s13131-021-1765-7
Marinov I, Follows M, Gnanadesikan A, et al. 2008. How does ocean biology affect atmospheric pCO_2? Theory and models. Journal of Geophysical Research: Oceans, 113(C7): C07032, doi: 10.1029/2007jc004598
Martin J H, Fitzwater S E, Gordon R M. 1990a. Iron deficiency limits phytoplankton growth in Antarctic waters. Global Biogeochemical Cycles, 4(1): 5–12, doi: 10.1029/GB004i001p00005
Martin J H, Gordon R M, Fitzwater S E. 1990b. Iron in Antarctic waters. Nature, 345(6271): 156–158, doi: 10.1038/345156a0
Mazloff M R, Heimbach P, Wunsch C. 2010. An eddy-permitting Southern Ocean state estimate. Journal of Physical Oceanography, 40(5): 880–899, doi: 10.1175/2009jpo4236.1
Mcgillicuddy D J, Sedwick P N, Dinniman M S, et al. 2015. Iron supply and demand in an Antarctic shelf ecosystem. Geophysical Research Letters, 42(19): 8088–8097, doi: 10.1002/2015gl065727
Medina-Gómez I, Trujillo A A, Marino-Tapia I, et al. 2019. Phytoplankton responses under a joint upwelling event and an algal bloom scenario in the southeast Gulf of Mexico. Continental Shelf Research, 184: 30–43, doi: 10.1016/j.csr.2019.07.006
Mitchell B G, Brody E A, Holm-Hansen O, et al. 1991. Light limitation of phytoplankton biomass and macronutrient utilization in the Southern Ocean. Limnology and Oceanography, 36(8): 1662–1677, doi: 10.4319/lo.1991.36.8.1662
Moline M A, Claustre H, Frazer T K, et al. 2004. Alteration of the food web along the Antarctic Peninsula in response to a regional warming trend. Global Change Biology, 10(12): 1973–1980, doi: 10.1111/j.1365-2486.2004.00825.x
Moore J K, Abbott M R. 2000. Phytoplankton chlorophyll distributions and primary production in the Southern Ocean. Journal of Geophysical Research: Oceans, 105(C12): 28709–28722, doi: 10.1029/1999JC000043
Moore J K, Doney S C, Glover D M, et al. 2001. Iron cycling and nutrient-limitation patterns in surface waters of the world ocean. Deep Sea Research Part II: Topical Studies in Oceanography, 49(1–3): 463–507, doi: 10.1016/S0967-0645(01)00109-6
Moore J K, Doney S C, Lindsay K. 2004. Upper ocean ecosystem dynamics and iron cycling in a global three-dimensional model. Global Biogeochemical Cycles, 18(4): GB4028, doi: 10.1029/2004gb002220
Pang Shanshan, Wang Xidong, Liu Hailong, et al. 2019. Decadal variability of the barrier layer and forcing mechanism in the Bay of Bengal. Journal of Geophysical Research: Oceans, 124(7): 5289–5307, doi: 10.1029/2018jc014918
Park J, Oh I S, Kim H C, et al. 2010. Variability of SeaWiFs chlorophyll-*a* in the southwest Atlantic sector of the Southern Ocean: strong topographic effects and weak seasonality. Deep-Sea Research Part I: Oceanographic Research Papers, 57(4): 604–620, doi: 10.1016/j.dsr.2010.01.004
Pauly D, Christensen V. 1995. Primary production required to sustain global fisheries. Nature, 374(6519): 255–257, doi: 10.1038/374255a0
Qiu Yun, Cai Wenju, Li Li, et al. 2012. Argo profiles variability of barrier layer in the tropical Indian Ocean and its relationship with the Indian Ocean Dipole. Geophysical Research Letters, 39(8): L08605, doi: 10.1029/2012gl051441
Sallée J B, Speer K G, Rintoul S R. 2010. Zonally asymmetric response of the Southern Ocean mixed-layer depth to the southern annular mode. Nature Geoscience, 3(4): 273–279, doi: 10.1038/ngeo812
Schueler C F, Clement J E, Ardanuy P E, et al. 2002. NPOESS VIIRS sensor design overview. In: Proceedings of SPIE 4483, Earth Ob-

serving Systems VI. San Diego, CA, USA: SPIE, 11–23, doi: 10.1117/12.453451

Shi Yuxin, Liu Hailong, Wang Xidong, et al. 2024. Responses of the southern ocean mixed layer depth to the eastern and central Pacific El Niño events during austral winter. Acta Oceanologica Sinica, 43(7), doi: 10.1007/s13131-023-2228-0

Smith W O Jr, Comiso J C. 2008. Influence of sea ice on primary production in the Southern Ocean: a satellite perspective. Journal of Geophysical Research: Oceans, 113(C5): C05S93, doi: 10.1029/2007jc004251

Sverdrup H U. 1953. On conditions for the vernal blooming of phytoplankton. ICES Journal of Marine Science, 18(3): 287–295, doi: 10.1093/icesjms/18.3.287

Tagliabue A, Sallée J B, Bowie A R, et al. 2014. Surface-water iron supplies in the Southern Ocean sustained by deep winter mixing. Nature Geoscience, 7(4): 314–320, doi: 10.1038/ngeo2101

Taylor J R, Ferrari R. 2011. Ocean fronts trigger high latitude phytoplankton blooms. Geophysical Research Letters, 38(23): L23601, doi: 10.1029/2011gl049312

Thomalla S J, Fauchereau N, Swart S, et al. 2011. Regional scale characteristics of the seasonal cycle of chlorophyll in the Southern Ocean. Biogeosciences, 8(10): 2849–2866, doi: 10.5194/bg-8-2849-2011

Tripathy S C, Pavithran S, Sabu P, et al. 2015. Deep chlorophyll maximum and primary productivity in Indian Ocean sector of the Southern Ocean: case study in the subtropical and polar front during austral summer 2011. Deep-Sea Research Part II: Topical Studies in Oceanography, 118: 240–249, doi: 10.1016/j.dsr2.2015.01.004

Venables H, Moore C M. 2010. Phytoplankton and light limitation in the Southern Ocean: learning from high-nutrient, high-chlorophyll areas. Journal of Geophysical Research: Oceans, 115(C2): C02015, doi: 10.1029/2009jc005361

Verdy A, Mazloff M R. 2017. A data assimilating model for estimating Southern Ocean biogeochemistry. Journal of Geophysical Research: Oceans, 122(9): 6968–6988, doi: 10.1002/2016jc012650

Ying Meijia, Liu Hailong, Wang Fuchang, et al. 2019. Spatio-temporal variations of mixed layer depth in Southern Ocean. Oceanologia et Limnologia Sinica (in Chinese), 50(6): 1223–1232, doi: 10.11693/hyhz20190800153